# Modulating $D_{33}$ Coefficients Through In Situ AgF and Ag$_2$O Growth in PVDF Composites for High-Performance Piezoelectric Nanogenerators

*Renjun Liu, Ki Hoon Shin, Yu Zhu, Qing Liu, Bing Ji, Guoxing Sun, Zongjin Li,\* Dadimuni De Silva, Aisling Stewart, Matteo Lorenzoni, Ingo Ludtke, Oliver A. Williams, Wenlong Ming, Giorgio Divitini,\* Jung Inn Sohn,\* and Bo Hou\**

Polyvinylidene fluoride (PVDF) membranes, known for their flexibility, biocompatibility, and piezoelectricity, hold significant promise for energy harvesting applications in bioelectronics. Enhancing the $\beta$-phase content is critical for improving device performance. This study presents an effective strategy to boost the relative concentration of $\beta$-PVDF through the in situ growth of silver(I) fluoride (AgF) and silver oxide (Ag$_2$O) nanoparticles (NPs). By optimizing the concentration of NPs, the $\beta$-phase content in PVDF composite films increased to 91.4%. Dielectric analysis revealed a remarkable enhancement of the dielectric constant, reaching 30.1—over three times higher than that of pristine PVDF at 1000 Hz. Additionally, the piezoelectric coefficient of the optimized PVDF composite film improved by 50%, reaching $\approx$12 pC N$^{-1}$. A prototype nanogenerator based on the optimized composite film achieved an open-circuit voltage of $\approx$35 V, a short-circuit current of $\approx$1.6 µA, and an output power density of $\approx$25 µW cm$^{-2}$ under 0.5 MPa compressive stress. The device successfully powered 10 blue LEDs and charged a 50 nF capacitor within 10 s. These findings highlight in-situ growth of silver-based nanoparticle in PVDF matrix provides a scalable approach for energy harvesting and storage technologies.

## 1. Introduction

Piezoelectric materials have been extensively studied for widespread applications in various areas, such as energy harvesters, self-powered sensors, smart skins, and wearable electronics.[1–6] The typical inorganic ferroelectric materials, like barium titanate BaTiO$_3$ (BTO) and lead zirconate titanate PbZr$_x$Ti$_{1-x}$O$_3$ (PZT), have attracted considerable attention and have already obtained great commercial success due to their excellent piezoelectric properties such as high piezoelectric coefficient ($d_{33}$) and high dielectric constant ($\varepsilon_r$),[7–14] which make them widely employed in the fields of energy storage, holography and strain sensing. However, the rigidity, brittleness, complicated processing, and inclusion of toxic elements, such as lead, have limited their further application, particularly in bioelectronics.[15,16,17]

R. Liu, D. De Silva, A. Stewart, O. A. Williams, B. Hou
School of Physics and Astronomy
Cardiff University
Queen's Buildings North Building
The Parade, Newport Road, Cardiff, Wales CF24 3AA, UK
E-mail: houb6@cardiff.ac.uk

R. Liu, G. Sun, Z. Li
Joint Key Laboratory of the Ministry of Education
Institute of Applied Physics and Materials Engineering
University of Macau
Avenida da Universidade, Taipa, Macau 58816, China
E-mail: zjli@must.edu.mo

K. H. Shin, J. I. Sohn
Division of Physics and Semiconductor Science
Dongguk University-Seoul
Seoul 04620, Republic of Korea
E-mail: junginn.sohn@dongguk.edu

Y. Zhu
Henan Key Laboratory of Materials on Deep-Earth Engineering
School of Materials Science and Engineering
Henan Polytechnic University
Jiaozuo, Henan 454000, China

A polymer-based material such as poly(vinylidene fluoride) (PVDF) is an attractive alternative, due to its low density, flexibility, biocompatibility, and excellent pyro-, piezo-, and ferroelectric properties.[18–23] Moreover, the presence of five crystalline phases ($\alpha$, $\beta$, $\gamma$, $\delta$, and $\varepsilon$) opens up several opportunities for tuning the material, enabling excellent mechanical properties, high thermal and chemical stabilities;[24–26] particularly, the polar $\beta$-phase is desirable in the field of piezotronics. Unfortunately, typical synthesis routes for PVDF powder result in the nonpolar $\alpha$-phase. Converting the nonpolar phase to the polar phase PVDF is necessary to achieve an excellent piezoelectric response. The typical way to accomplish this goal is to dissolve PVDF powder into polar solvents such as dimethylformamide (DMF) and dimethyl sulfoxide (DMSO), then cast the PVDF solution on a glass substrate to form a PVDF membrane using a solvent cast or spin coating method, and finally polarize the membrane using techniques such as field poling,[27] corona poling,[28] stretching,[29] and heat pressing.[30] However, the content of $\beta$-PVDF by these methods is still not high enough.

A promising way to promote the $\beta$-phase is by loading nontoxic fillers into the PVDF matrix. Fillers with nanoparticle structures, such as our previous works on colloidal quantum dots[21–23] and other previous reports on graphite oxide (GO),[31] multi-walled carbon nanotubes (MW-CNT),[32] and zinc oxide (ZnO),[33] have been successfully proven to utilize or boost the content of $\beta$-PVDF in composite films and thus generating piezoelectric field or enhancing the piezoelectric coefficient and dielectric constant. Energy harvesting devices based on these composite films have obtained high output voltage and current density. Besides, the devices bring better performances after they are under electrical poling treatment. However, the typical process for loading the fillers into the PVDF matrix is via mechanical mixing, which can lead to their aggregation and an inhomogeneous distribution in the composite films, thus degrading performance. In situ, loading of the fillers into the matrix effectively solves the issue of uneven distribution. For example, using silver nitrate ($AgNO_3$) as a precursor, Ag nanoparticles (NPs) were used as fillers in the literature due to their high electrical and thermal conductivity, effective anti-bacterial/anti-fouling action, and relatively low cost.[34–38] However, the boosting effect for the $\beta$-PVDF phase in PVDF composite films is very limited, only using Ag nanoparticles has been reported so far.

In this work, a method has been developed to enhance the polar $\beta$-PVDF composite film by in situ loading AgF and $Ag_2O$ NPs using $AgNO_3$ as the precursor. Through this method, the NPs can be uniformly dispersed in the composite film, thus leading to a better overall performance. Furthermore, by tuning the loading concentration of $AgNO_3$, the optimal concentration can be obtained for the composite film, resulting in a 91.4% fraction of the $\beta$-PVDF phase. Moreover, a 50% increase of $d_{33}$ can be achieved compared to the pristine PVDF film. The performance of the obtained films for energy harvesting has been investigated. The electrical output of a piezoelectric device based on PVDF composite film with optimized loading can reach ≈35 V, 1.6 µA, and 25 µW cm$^{-2}$, for open circuit voltage, short circuit current and output power density, respectively. As a proof-of-concept, the piezoelectric nanogenerator could rapidly charge a 50 nF capacitor to a saturated voltage state and power 10 commercial blue light LEDs.

## 2. Results and Discussion

### 2.1. The Morphology Study of PVDF Composite Films

A batch of experiments was developed to find the optimal content that efficiently enhances the polar phase of PVDF. First, $AgNO_3$ with different mass ratios (0, 0.22, 0.58, 1.2, 1.5, 2.1, 3.4 and 5.6 wt%) was added to a PVDF (DMF) solution with a concentration of 120 mg mL$^{-1}$ to prepare the composite films. The processes are briefly illustrated in **Figure 1a**. After that, the surface morphologies of samples with $AgNO_3$ loading concentrations of 0, 1.5, and 5.6 wt% were mapped as shown in Figure 1b–d. A porous structure appears on the surface with the increased loading concentration of $AgNO_3$. Moreover, the density and size of the pores increase for the samples with higher loading concentrations, as can be observed in large-area images of the whole samples shown in Figure S1 (Supporting Information). It should also be noted that the pristine sample tends to present cracks (0 wt%, Figure 1b); the addition of NPs prevents such cracking already at low loading, as shown in Figure S1b (Supporting Information). Furthermore, the nanoparticles (NPs) formed in the composite films in the control experiments are present on the surface of the composite films. The NPs size is in the range of 50–150 nm. The generated NPs in the PVDF matrix play an important role not only in modifying the morphology of composite films but also in promoting $\beta$-PVDF which will be addressed later.

Next, to explore the distribution of the in situ growth of NPs, the SEM-EDS mapping of the top surface and cleaved cross-sections of the samples was conducted. It is clear from Figure S3 (Supporting Information) that all the major elements are present, with F and C from PVDF, and O and Ag from $AgNO_3$. Since these

Q. Liu
Department of Civil and Environmental Engineering
National University of Singapore
Singapore 117576, Singapore

B. Ji
Key Laboratory of Low Dimensional Quantum Structures and Quantum Control
School of Physics and Electronics
Hunan Normal University
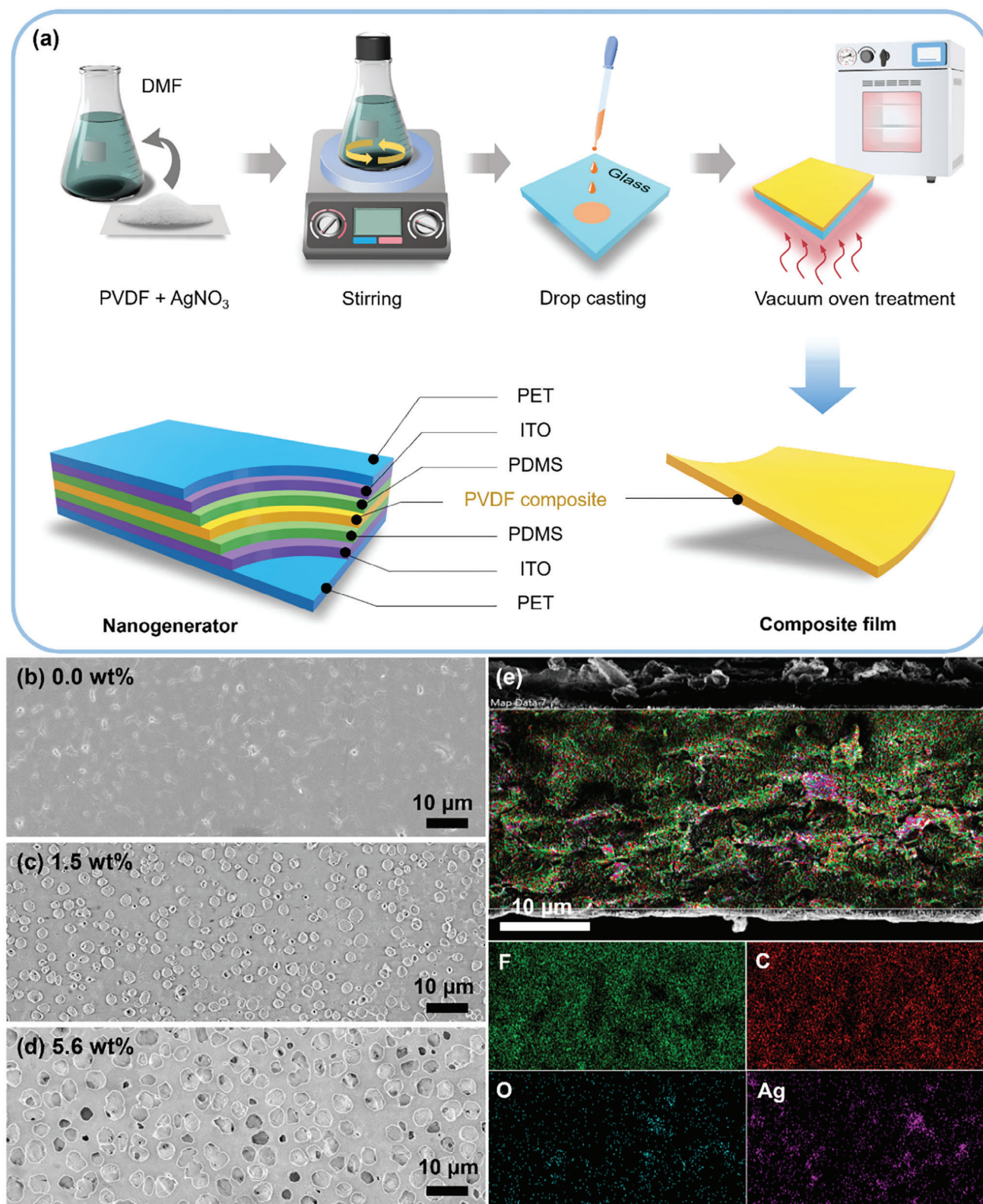No. 36 Lushan Road, Changsha, Hunan 410081, China

Z. Li
Faculty of Innovation Engineering
Macau University of Science and Technology
Avenida Wai Long, Taipa, Macao SAR 999078, China

D. De Silva
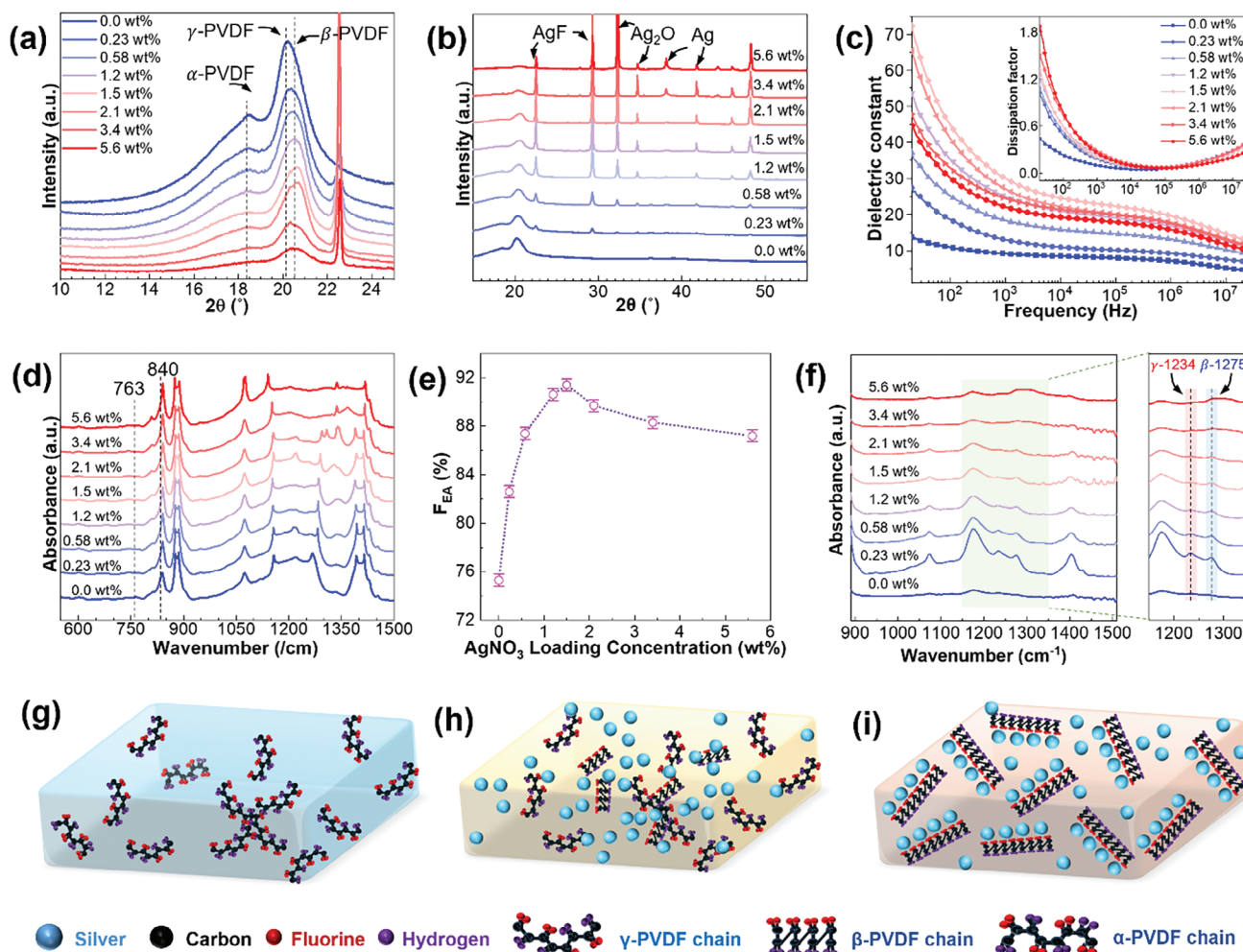Department of Engineering
University of Cambridge
Trumpington Street, Cambridge CB2 1PZ, UK

A. Stewart, W. Ming
School of Engineering
Cardiff University
Cardiff CF24 3AA, UK

M. Lorenzoni, G. Divitini
Istituto Italiano di Tecnologia
via Morego 30, Genoa 16163, Italy
E-mail: Giorgio.Divitini@iit.it

I. Ludtke, W. Ming, B. Hou
Compound Semiconductor Applications Catapult
Newport NP108BE, UK

**Figure 1.** a) Schematics of the fabrication processes of PVDF composite films and free-standing composite films. PVDF and $AgNO_3$ are dissolved in DMF, the mixed solution is stirred, drop cast on glass substrates, and dried in a vacuum oven. Flexible free-standing PVDF composite films are peeled from the glass substrate and finally assembled into a piezoelectric nanogenerator. b–d) SEM images of samples with different loadings of $AgNO_3$ (0, 1.5, and 5.6 wt% respectively). With the increase of $AgNO_3$ loading, pores appear, with density and size increasing for higher loadings. e) SEM-EDS compositional maps for a cleaved cross-section of the composite film. Elements C and F are from the PVDF matrix, while O and Ag are from $AgNO_3$.

**ADVANCED
SCIENCE NEWS**

www.advancedsciencenews.com

**ADVANCED
MATERIALS
TECHNOLOGIES**

www.advmattechnol.de

**Figure 2.** a, b) X-ray diffraction patterns of PVDF composite films with different AgNO$_3$ loadings (0, 0.23, 0.58, 1.2, 1.5, 2.1, 3.4 and 5.6 wt%). c) Dielectric constant and dissipation factor (inset) as a function of frequency for PVDF composite films. d) FTIR absorption of PVDF composite films. e) Content of the electroactive phase as a function of AgNO$_3$ loading. f) ATR–FTIR absorption band of PVDF composite films with different AgNO$_3$ loadings. g–i) Proposed mechanism of $\gamma$-PVDF conversion to $\beta$-PVDF in the presence of Ag$^+$. g) Without AgNO$_3$, $\gamma$-PVDF is the dominant phase. h) With a low AgNO$_3$ loading, Ag$^+$ starts to interact with F$^-$, and part of $\gamma$-PVDF is converted into $\beta$-PVDF; the composite film turns to shallow yellow. i) With a high enough AgNO$_3$ loading, $\beta$-PVDF becomes the dominant phase, and the composite film turns dark brown.

elements (O and Ag) give a uniform distribution on the surface of the composite film, it is reasonable to imply that the NPs are uniformly distributed, showing that in situ growth of NPs is effective. In addition, from cross-sectional mapping, as shown in Figure 1e, we can see that the thickness of the composite film is ≈30 µm and silver is distributed throughout the entire film. The cleavage is not smooth due to the breaking of the porous structures. Therefore, we can make the reasonable assumption that the porous network structures are continuous inside the composite film, which is of great significance to the enhancement of the piezoelectric performance of the composite film and the related device. There are two possible reasons behind this. First, a porous composite film is beneficial for coupling strain when an appropriate external compressive force is applied. Thus, strain can lead to a significant output device performance.[39,40] Second, due to the pores, the composite film can be treated as a large number of micro-capacitors connected in series and parallel, which is advantageous for electric energy storage converted from mechanical energy.[41] Also, it is worth noting the contrast in the SEM images presents bright features – as can be seen from the elemental maps, these do not necessarily indicate Ag-rich areas, but rather originate from topographic contrast, particularly strong in areas where the cleaving process left rough edges.

### 2.2. The X-Ray Crystallography Study of PVDF Composite Films

To further determine the component of the NPs, the X-ray diffraction measurements were conducted for the composite films with different loading concentrations of AgNO$_3$ (0, 0.23, 0.58, 1.2, 1.5, 2.1, 3.4 and 5.6 wt%). The results are shown in **Figure 2a,b**. It can be seen from Figure 2a that with the increased loading, the diffraction peak of PVDF shifts from 20.2° to 20.6°, which are characteristic of $\gamma$-PVDF and $\beta$-PVDF, respectively. Also, at 0 wt%

**ADVANCED
SCIENCE NEWS**

www.advancedsciencenews.com

**ADVANCED
MATERIALS
TECHNOLOGIES**

www.advmattechnol.de

loading (pristine PVDF film), the $\gamma$-PVDF is the dominant phase, with a small portion of $\alpha$-PVDF ($2\theta = 18.4°$). However, when the loading is equal to and higher than 1.5 wt%, the $\beta$-phase dominates. This means that the loading of AgNO$_3$ facilitates the conversion of $\gamma$-PVDF to $\beta$-PVDF.

Moreover, the diffraction peak of $\alpha$-PVDF becomes gradually lower and broader with the increased loading, which indicates that the loading of AgNO$_3$ can suppress the $\alpha$-PVDF phase. Therefore, it is concluded that the loading of AgNO$_3$ can promote the transformation from $\gamma$-PVDF to $\beta$-PVDF. Furthermore, it can be seen from Figure 2b that two major peaks appear at 22.5° and 29.3° for the sample at a low loading content (0.23 wt%). The peaks indicate the formation of AgF NPs.[42] The colour of AgF is yellow,[43] which is consistent with the colour of the corresponding composite film, as shown in Figure S4 (Supporting Information). The composite film is light yellow since the AgF NPs content is relatively small. However, the AgF enhances the formation of $\beta$-PVDF, because the peak position of the sample (0.23 wt%) is shifted to a large value compared with the pristine PVDF sample. The trend of the shift becomes clearer with the increasing formation of AgF NPs, as shown in Figure 2a. A possible cause for the enhancement of $\beta$-PVDF can be the strong electronegativity of F⁻, which can interact with the Ag⁺ in the solution forcing the structure of PVDF to transform from the TGTG arrangement to the TTTT arrangement. The process can be further illustrated from Figure 2g–i. Moreover, further increasing the concentration of AgNO$_3$ (above 0.58 wt%) improves the formation of AgF NPs; therefore, the colour of the corresponding samples varies from light yellow to deep yellow, and the X-ray diffraction signal for AgF becomes stronger, as shown in Figure 2b. In addition, it is clear that with the increase of loading of AgNO$_3$, another primary diffraction line at a $2\theta$ value of 32.5° becomes stronger. This feature originates from Ag$_2$O NPs, which are stable and black or dark brown,[44] and a p-type semiconductor with a bandgap energy of ≈1.4 eV.[45] This explains why the colour of samples changes from deep yellow to dark brown, especially at high loadings (larger than 3.4 wt%). The black Ag$_2$O NPs are responsible for the "dark" component in the composite films. At low AgNO$_3$ loading (0.23 wt%), the contribution of Ag$_2$O NPs to $\beta$-PVDF is not obvious. However, when the loading of AgNO$_3$ is equal to or larger than 3.4 wt%, the diffraction peaks of $\gamma$- and $\beta$-PVDF are broadened. A possible explanation is that more NPs are generated and tend to aggregate, degrading the crystallinity of PVDF at higher AgNO$_3$ loading concentrations.

It is worth mentioning that although pure Ag particles are formed at higher loading concentrations of AgNO$_3$, their total content is relatively small. Also, due to the aggregation effect of AgF and Ag$_2$O NPs, the contribution of Ag particles to the formation of $\beta$-PVDF is not obvious. Therefore, the following conclusions can be reached from the above discussion: AgNO$_3$, as an ionic compound, can boost the polar phase of PVDF. Among the NPs formed in the composite films, AgF NPs are the main contributor to the formation of the polar phase. Especially at a low loading of AgNO$_3$ (0.23 wt%), the AgF NPs are the main compound formed. At higher values, the generated Ag$_2$O NPs join the boosting process of the formation of $\beta$-PVDF together with AgF NPs. The conclusion can be further strengthened by Figure S5 (Supporting Information). In Figure S5a (Supporting Information), with the increase of AgNO$_3$ loading concentration, the

binding energy of the Ag element tends to shift to a lower value. Moreover, the binding energy of the Ag element is the highest at an AgNO$_3$ loading concentration of 0.23 wt%, which shows that the primary product is AgF NPs instead of Ag$_2$O. This is because the chemical bond of Ag-F is stronger than that of Ag-O, since the electronegativity of F is larger than that of O, leading to a stronger interaction of Ag and F. However, with the further increase of AgNO$_3$ concentration, the content of Ag$_2$O NPs gradually begins to increase, which leads to the decrease of bonding energy of Ag. Furthermore, from Figure S5b (Supporting Information), we can see that at a low AgNO$_3$ loading of 0.23 wt%, the absorption bands are mainly from AgF NPs. This is because the absorption cut-off wavelength for Ag$_2$O NPs is ≈885 nm. But from 650 to 800 nm, there is almost no absorption in the spectrum, showing that the content of Ag$_2$O NPs is extremely low and that the absorption can be neglected. However, with further loading of AgNO$_3$, the content of Ag$_2$O NPs increases. As a consequence, strong absorption from Ag$_2$O NPs is observed.

## 2.3. FTIR Study of PVDF Composite Films

Fourier transform infrared (FTIR) spectrometer was employed to measure the crystalline phases of the specimens. The characteristic absorption band for $\alpha$-phase PVDF is typically 763 cm⁻¹, and the absorption band of the electroactive phase (including $\beta$- and $\gamma$-PVDF) is 840 cm⁻¹. The results are shown in Figure 2d. It is obvious that the electroactive phase with absorption bands at 840 cm⁻¹ dominated the spectrum compared with the nonpolar $\alpha$-PVDF with absorption bands at 763 cm⁻¹, which is under extreme suppression. The percentage content of the electroactive phase in PVDF can be calculated by the Gregorio equation:[46]

$$F_{EA} = \frac{A_{840}}{(X_{840}/X_{763})A_{763} + A_{840}} = \frac{A_{840}}{1.26A_{763} + A_{840}} \quad (1)$$

whereas $A_{763}$ and $A_{840}$ are the characteristic absorption intensity for $\alpha$-phase and electroactive phase, respectively. $X_{763}$ and $X_{840}$ are absorption coefficients with values of $6.1 \times 10^4$ and $7.7 \times 10^4$ cm² mol⁻¹, respectively. Figure 2e shows the calculated results for the content of the electroactive phase from Equation (1). The content of the electroactive phase increases, reaching an optimal value, and then slightly decreases with the increase of AgNO$_3$ loading. The result shows that the optimal loading of AgNO$_3$ is 1.5 wt%, and the corresponding content of the electroactive phase is as high as 91.4%. However, due to strong absorption for the composite film at 1234 and 1275 cm⁻¹, which respectively correspond to $\gamma$- and $\beta$-PVDF absorption bands, the measurement is out of scope for the FTIR based on the method of transmission measurement. Therefore, ATR-FTIR was employed to conduct the measurement in this range, and the result is shown in Figure 2f. It can be seen that the $\gamma$- and $\beta$-PVDF phases are competing with each other, with more $\beta$-PVDF for increased AgNO$_3$ loading. At low loading (0.23–0.58 wt%), although $\beta$-PVDF is boosted and the absorption band is prominent, $\gamma$-PVDF is still the dominant phase. In this situation, the total content of the electroactive phase can be regarded as the content of $\gamma$-PVDF.[34,47] When the concentration increases to 1.2 wt%, the contents of $\gamma$- and $\beta$-PVDF are almost

**ADVANCED
SCIENCE NEWS**

www.advancedsciencenews.com

**ADVANCED
MATERIALS
TECHNOLOGIES**

www.advmattechnol.de

equal. When concentration further increases to 2.1 wt%, $\beta$-PVDF becomes the dominant phase. In this situation, the total content of the electroactive phase can be regarded as the content of $\beta$-PVDF.[47] However, when the loading concentration of $AgNO_3$ is equal to or larger than 3.4 wt%, the absorption band for $\gamma$-PVDF is flattened and not clearly visible, and only $\beta$-PVDF can be identified. However due to a large number of formed NPs and the aggregation effect of NPs, the absorption band broadened, which is consistent with the XRD result in Figure 2b.

### 2.4. Dielectric Study of PVDF Composite Films

Since $\varepsilon_r$ of PVDF composite films is one of the critical parameters that contribute to $d_{33}$ due to the relationship ($d_{33} \propto \varepsilon_r \cdot P_r$, $P_r$ is remnant polarization), $\varepsilon_r$ was measured for composite films with different $AgNO_3$ loading. As shown in Figure 2c, $\varepsilon_r$ shows a tendency to increase with the increase of $AgNO_3$ loading from 0.23 to 1.5 wt%, which can be attributed to the formation of $\beta$-PVDF and the suppression of $\alpha$-PVDF. Since $\beta$-PVDF is a polar phase while $\gamma$-PVDF is a semi-polar phase, the contribution of $\beta$-PVDF to $\varepsilon_r$ is larger than that of $\gamma$-PVDF; $\alpha$-PVDF is a nonpolar phase with no contribution to $\varepsilon_r$. On the other hand, the $Ag_2O$ is a p-type semiconductor that can form interfacial polarization with the PVDF matrix. This can also contribute to $\varepsilon_r$, especially at low frequencies (< 100 Hz), which is consistent with the observation in Figure 2c. When the loading of $AgNO_3$ further increases from 2.1 to 5.6 wt%, $\varepsilon_r$ tends to decrease, which is mainly owing to the aggregation of generated NPs with high content. The dissipation factors ($\sigma$) of PVDF composite films tend to be slightly higher compared to the pure PVDF film even in the low-frequency domain (<1000 Hz), especially for the optimal loading concentration (1.5 wt%), as the inset shows in Figure 2c, with $\sigma$ ranging from 0.25 to 1.35. This means the optimal composite film can be a good candidate for application to energy storage devices. Also, it is worth noting that at a higher frequency (larger than 1000 Hz), $\sigma$ is lower than 0.5, which shows that the composite film has the potential to detect vibration with a high-frequency signal. Subsequently, the impedance characteristics of PVDF composite films were measured. Figure S6 (Supporting Information) shows the response of impedance and phase angle to frequency for PVDF composite films at different $AgNO_3$ loadings. It is clear from Figure S6a (Supporting Information) that the impedances of the composite films decrease with the increase of frequency $\omega$, indicating that the composite films have a property similar to capacitive reactance $X_C$, $X_C = 1/(\omega \cdot C)$. This can be further confirmed by the phase angle graph in Figure S6b (Supporting Information), where the phase angle is from $-90°$ to $-30°$. For a pure capacitor, the phase of the voltage signal lags $90°$ behind the phase of the current signal, whereas for a pure resistor, the phase is coherent. Consequently, composite films can be considered equivalent to a resistor and a capacitor connected in series. Compared with the value of the capacitor in this specific situation, the value of the resistor is very small and thus can be ignored. So, this is an indication that the composite films with a porous structure due to the presence of NPs produce a capacitive effect and can therefore be used as energy storage devices. Furthermore, with the increase of $AgNO_3$ loading from 0.23 to 2.1 wt%, the impedance tends to decrease, showing that loading of

$AgNO_3$ is beneficial to improve the conductivity of the composite films. This can be attributed to the increased content of $Ag_2O$ NPs due to their p-type semiconductivity.

### 2.5. The Piezoelectric Properties of PVDF Composite Films

$D_{33}$ is an important figure of merit in assessing the piezoelectricity of PVDF composite films. To further explore the piezoelectric properties, piezoelectric force microscopy (PFM) was used to map the piezoelectric performance of the free-standing composite films with $AgNO_3$ loading of 0 (pristine), 1.2, 3.4, and 5.6 wt%, respectively. The sample preparation process is as follows: first, a thickness of 100 nm of silver was thermal evaporated on one side of the free-standing composite films. Second, the as-prepared samples with a silver-deposited side were firmly glued to glass substrates using conductive tapes for the collection of electrical signals. The results are shown in **Figures 3** and **S7** (Supporting Information). From topographical images in Figure 3a–d, we can see the surface roughness tends to increase with the loading of $AgNO_3$. PVDF piezoelectric coefficient is generally not constant at different bias voltages, in our case the piezoelectric response tends to increase with the applied alternating voltage ($V_{ac}$) at $V_{ac}$ of 0.35 and 0.85 V, as shown in Figure 3e–h and Figure S7 (Supporting Information). Besides, the piezoelectric response of the sample loaded with $AgNO_3$ is larger than that of the pristine sample at the same $V_{ac}$. The $d_{33}$ can be extrapolated from piezoelectric responses using the following equation:

$$A = d_{33} V_{ac} Q \tag{2}$$

whereas A is the piezoelectric displacement, and Q is the Q-factor of the cantilever. The results are shown in Figure 3i and Figure S8 (Supporting Information). The $d_{33}$ has a value of $\approx 12$ pm V$^{-1}$ compared to that of the pristine sample with a value of $\approx 8$ pm V$^{-1}$, which shows that a boosting factor of $\approx 50\%$ of $d_{33}$ can be achieved for the PVDF composite film due to the effective loading of $AgNO_3$.

### 2.6. The Application of PVDF Composite Films in Nanogenerators

After a comprehensive study of $AgNO_3$-loaded PVDF composite films, including morphology, crystallography, and dielectric, electric and piezoelectric properties, we investigate applications for the composite film. One of the possible applications is an energy harvester based on the piezoelectric effect. To prove this, nanogenerators were fabricated based on composite films with different $AgNO_3$ loadings (0, 0.23, 0.58, 1.2, 1.5, 2.1, 3.4 and 5.6 wt%). The architecture of the generators was PET/ITO/PDMS/composite films/PDMS/ITO/PET, as shown in **Figure 4a**. Electric poling treatments were conducted for all of the devices under an electric field of $\approx 30$ kV for 2 h. The circuit for testing device performance is shown in Figure 4g and the details can be obtained in Video S2 (Supporting Information). The open circuit voltage was measured under the same external force of 0.5 MPa for nanogenerators with composite films at different loadings of $AgNO_3$. The results are shown in Figure 4b.
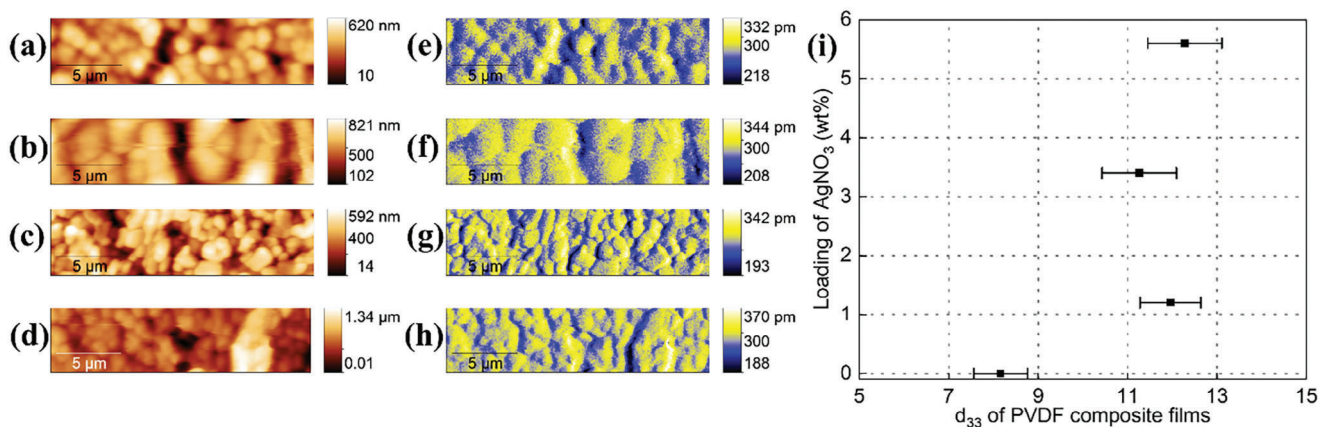
**Figure 3.** Piezoelectric performance of samples with different loading of AgNO$_3$. a–d) PFM images of topography for samples with loading of 0, 1.2, 3.4, and 5.6 wt%. e–h) PFM images of piezo displacement for samples with the loading of 0, 1.2, 3.4, and 5.6 wt% at a V$_{ac}$ of 0.85 V. i) The relationship of d$_{33}$ versus the loading of AgNO$_3$.
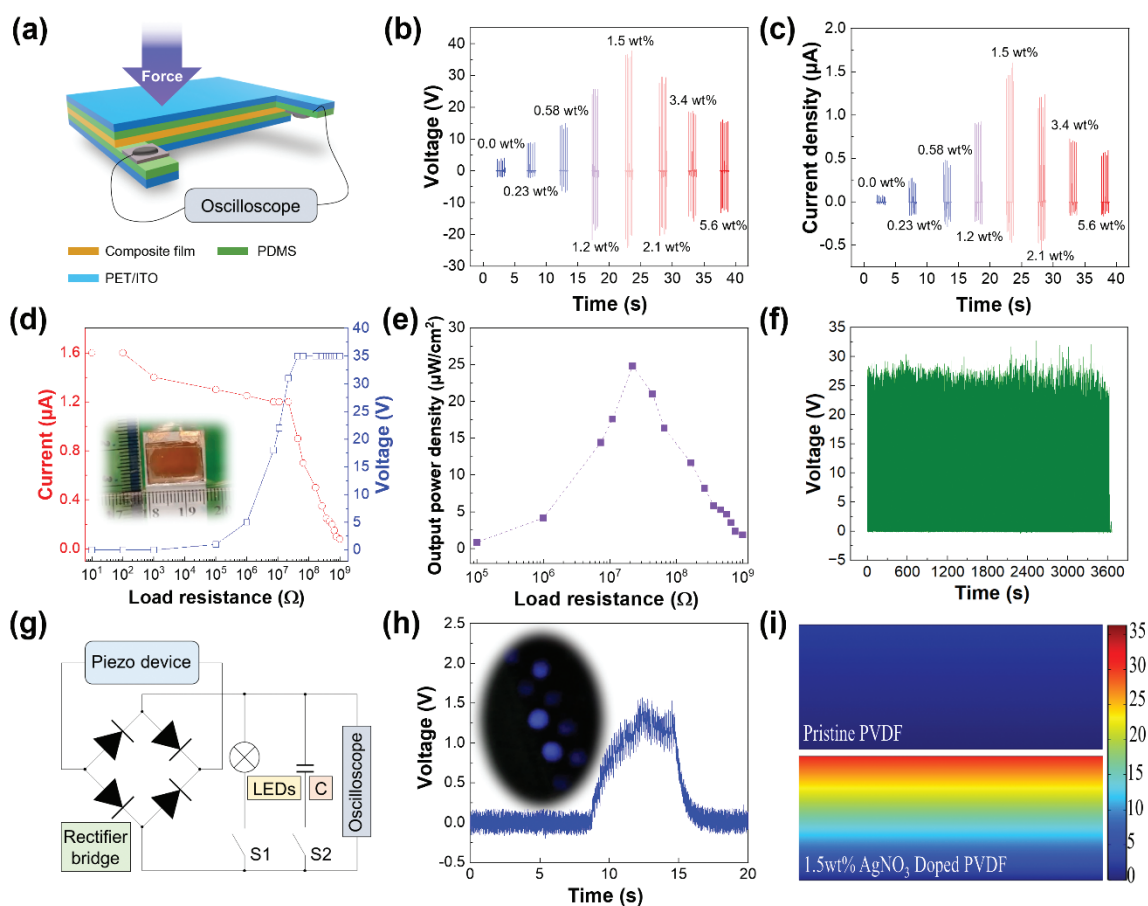


**Figure 4.** a) Schematics of nanogenerators based on PVDF composite films with different loadings. b) The open circuit output voltage and c) short circuit output current of nanogenerators based on different composite films. d) The output voltage and current of the nanogenerator with optimal loading at different electrical loading resistances. The inset reports a photograph of the nanogenerator. e) The output power density of the optimal nanogenerator at different loading resistances. f) The stability test of the optimal nanogenerator with an applied force of 0.5 MPa for more than 3600 s. g) The performance test electric circuit diagram of the piezoelectric device. h) The fast charge of a capacitor by the piezoelectric nanogenerator and inset digital image of 10 blue LEDs powered by the piezoelectric nanogenerator. i) COMSOL simulation of nanogenerators based on pure PVDF (Top) and 1.5 wt% AgNO$_3$ doped PVDF (Bottom). The colour bar values represent voltage (V).

**ADVANCED
SCIENCE NEWS**

www.advancedsciencenews.com

**ADVANCED
MATERIALS
TECHNOLOGIES**

www.advmattechnol.de

The output voltage begins to increase with the loading, reaching a maximum value of ≈35 V at an optimal value of 1.5 wt%, and then starting to decrease. This result is consistent with the FTIR absorption spectra and XRD diffraction patterns. Additionally, the conclusion is further strengthened by the simulation results from COMSOL as shown in Figure 4i. Besides, the forward connection and reverse connection test show the voltage output performance originates from the piezo effect as shown in Figure S8 (Supporting Information). Then, under the same test condition, the short circuit current was measured, and the result is shown in Figure 4c. The trend of current is similar to that of the voltage and the highest current is ≈1.6 µA. Next, the output performance of the optimal device (1.5 wt%) was measured under different load resistances. It is clear from Figure 4d that the nanogenerator can achieve the maximum output performance when the load resistance is ≈22 MΩ and the maximum output power density is ≈25 µW cm$^{-2}$ as shown in Figure 4e. Furthermore, a stability test of the generator was conducted under an applied force of 0.3 MPa for a test time of more than 3600 s. From Figure 4f we can see that the generator possesses excellent durability. In addition, the optimal nanogenerator was used to charge a capacitor with a capacitance value of 50 nF, with good charging efficiency, as shown in Figure 4h. It takes less than 10 s to charge the capacitor to a saturated state at ≈1.5 V, as shown in Video S1 (Supporting Information). Moreover, the output voltage of the optimal nanogenerator can be used to power 10 commercial blue light LEDs, as the inset shows in Figure 4h and Video S2 (Supporting Information), which shows that the nanogenerator based on the composite film has a potential application in mechanical energy harvesting.

## 3. Conclusion

A method of boosting the $\beta$-PVDF phase content in polymer films by the in situ growth of AgF and Ag$_2$O NPs has been developed. AgNO$_3$ with different weight ratios was loaded into PVDF to form composite films. It was found that the optimized composite film achieved a content of $\beta$-PVDF (91.4%) at 1.5 wt% concentration of AgNO$_3$ during the processing. The generated AgF and Ag$_2$O NPs are responsible for promoting the $\beta$-PVDF phase. The enhancement factor of d$_{33}$ of optimized PVDF composite film can achieve ≈50% compared to the pristine PVDF film. Piezoelectric nanogenerators based on composite films achieve good performance and can achieve an output power density of 25 µW cm$^{-2}$, power ten blue light LEDs and rapidly charge a capacitor. Our research shows that the AgF and Ag$_2$O co-doped PVDF composite films can be produced in a scalable, economical process and have great potential in flexible electronics, energy storage and energy harvesting applications.

## 4. Experimental Section

*Preparation of PVDF Composite Films*: PVDF powder (Mw ≈534000) was purchased from Alfa Aesar, and DMF (anhydrous, 99.8%) solvent was purchased from Sigma–Aldrich. First, the 120 mg mL$^{-1}$ PVDF solution was prepared by dispersing PVDF powder into the DMF solvent. Then, AgNO$_3$ with different mass weights was added to the DMF solvent, respectively. DMF was chosen as it is a strong polar solvent and can dissolve PVDF. After that, to have a better dispersion of PVDF and AgNO$_3$, the as-prepared

solution was stirred at 50 °C using a magnetic stirrer for 12 h in the dark. Then, after a 15 min ultrasonic treatment, the as-prepared solution went through a de-gassing process for 3 min in a vacuum oven. Subsequently, a composite film with a thickness of ≈30 µm was prepared by solution casting and baked in a vacuum oven drying at an optimized temperature for 2 h at 100 °C, followed by 5 h treatment at 135 °C. The piezoelectric nanogenerators were assembled by sandwiching the as-prepared PVDF composite films between two PET/ITO electrodes coated with PDMS (from Sylgard 184, Dow Corning, USA) with a thickness of ≈100 µm. The thickness of PET/ITO (from Sigma–Aldrich) was 127 µm, with the ITO layer thickness of 130 nm. The ITO sheet resistance was 60 Ω/□. Finally, to align dipoles, the devices were poled under a DC electric field with an intensity of ≈30 kV cm$^{-1}$ for 2 h at room temperature in ambient air.

*Characterization of PVDF Composite Films and Piezoelectric Devices*: The surface morphologies of PVDF composite films were mapped by field-emission scanning electron microscopy (Zeiss Sigma FESEM). The crystalline phase of the specimens was characterized by a Fourier transform infrared spectrometer (Bruker Tensor II) ranging from 600 to 1600 cm$^{-1}$ with a resolution of 4 cm$^{-1}$ and with an average scan number of 32 and an X-ray diffractometer (XRD) with monochromatic Cu-$\alpha$ radiation. The dielectric constant and dissipation factor, and the impedance of the composite films were measured by an impedance analyzer (Keysight E4990A) with a dielectric test fixture (Keysight 16451B). The output voltage of the piezoelectric generator was measured by a mixed signal oscilloscope (Tektronix 5 series) equipped with a differential probe (Tektronix THDP0200) with an input impedance of 10 MΩ. The output current of the piezoelectric generator was measured by a parameter analyzer (Keithley model 4200A-SCS). The piezoelectric performance at the nanoscale of PVDF composite films was measured using piezoresponse force microscopy (PFM),[48,49] scanning with 0.35 and 0.85 V$_{ac}$ on composite films, using a Pt-coated Si solid tip with a force constant of ≈1 N m$^{-1}$ and contact resonance ≈196 kHz. The measurements were conducted with imaging near contact resonance with the Dual AC Resonance Tracking (DART)[50] method on an MFP-3D AFM by Asylum research.

## Supporting Information

Supporting Information is available from the Wiley Online Library or from the author.

## Conflict of Interest

The authors declare no conflict of interest.

## Data Availability Statement

Information on the data underpinning this publication, including access details, can be found in the Cardiff University Research Data Repository at [DOI:10.17035/cardiff.28409627].

**ADVANCED**
**SCIENCE NEWS**

www.advancedsciencenews.com

**ADVANCED**
**MATERIALS**
**TECHNOLOGIES**

www.advmattechnol.de

[1] U. Yaqoob, A. S. M. I. Uddin, G. S. Chung, *Appl. Surf. Sci.* **2017**, *405*, 420.

[2] C. Sun, J. Shi, X. Wang, *J. Appl. Phys.* **2010**, *108*, 034309.

[3] J. H. Jung, M. Lee, J. I. Hong, Y. Ding, C. Y. Chen, L. J. Chou, Z. L. Wang, *ACS Nano* **2011**, *5*, 10041.

[4] N. A. Shepelin, A. M. Glushenkov, V. C. Lussini, P. J. Fox, G. W. Dicinoski, J. G. Shapter, A. V. Ellis, *Energy Environ. Sci.* **2019**, *12*, 1143.

[5] Y. Cho, S. Pak, G. H. An, B. Hou, S. Cha, *Isr. J. Chem.* **2019**, *59*, 747.

[6] Z. L. Wang, *Nanopiezotronics* **2007**, *19*, 889.

[7] L. Lu, W. Ding, J. Liu, B. Yang, *Nano Energy* **2020**, *78*, 105251.

[8] D. Hu, M. Yao, Y. Fan, C. Ma, M. Fan, M. Liu, *Nano Energy* **2019**, *55*, 288.

[9] W. Yan, G. Noel, G. Loke, E. Meiklejohn, T. Khudiyev, J. Marion, G. Rui, J. Lin, J. Cherston, A. Sahasrabudhe, J. Wilbert, I. Wicaksono, R. W. Hoyt, A. Missakian, L. Zhu, C. Ma, J. Joannopoulos, Y. Fink, *Nature* **2022**, *603*, 616.

[10] G. T. Hwang, V. Annapureddy, J. H. Han, D. J. Joe, C. Baek, D. Y. Park, D. H. Kim, J. H. Park, C. K. Jeong, K. I. Park, J. J. Choi, D. K. Kim, J. Ryu, K. J. Lee, *Adv. Energy Mater.* **2016**, *6*, 1600237.

[11] S. B. Seo, S. H. Lee, C. B. Yoon, G. T. Park, H. E. Kim, *J. Am. Ceram. Soc.* **2004**, *87*, 1238.

[12] Z. Zeng, Q. Wu, M. Hao, W. Lu, G. Fan, M. Yuchi, M. Ding, *J. Mater. Sci.: Mater. Electron.* **2018**, *29*, 8279.

[13] I. Fujii, K. Nakashima, N. Kumada, S. Wada, *J. Ceram. Soc. Jpn.* **2012**, *120*, 30.

[14] J. Lim, H. Jung, C. Baek, G. T. Hwang, J. Ryu, D. Yoon, J. Yoo, K. I. Park, J. H. Kim, *Nano Energy* **2017**, *41*, 337.

[15] A. C. Lopes, J. Gutiérrez, J. M. Barandiarán, *Eur. Polym. J.* **2018**, *99*, 111.

[16] F. R. Fan, W. Tang, Z. L. Wang, *Adv. Mater.* **2016**, *28*, 4283.

[17] C. Dagdeviren, B. D. Yang, Y. Su, P. L. Tran, P. Joe, E. Anderson, J. Xia, V. Doraiswamy, B. Dehdashti, X. Feng, B. Lu, R. Poston, Z. Khalpey, R. Ghaffari, Y. Huang, M. J. Slepian, J. A. Rogers, *Proc. Natl. Acad. Sci. USA* **2014**, *111*, 1927.

[18] A. Vinogradov, F. Holloway, *Ferroelectrics* **1999**, *226*, 169.

[19] B. Ameduri, *Chem. A Eur. J.* **2018**, *24*, 18830.

[20] J. Gomes, J. Serrado Nunes, V. Sencadas, S. Lanceros-Mendez, *Smart Mater. Struct.* **2010**, *19*, 065010.

[21] Y. Cho, P. Giraud, B. Hou, Y. W. Lee, J. Hong, S. Lee, S. Pak, J. Lee, J. E. Jang, S. M. Morris, J. I. Sohn, S. Cha, J. M. Kim, *Adv. Energy Mater.* **2018**, *8*, 1700809.

[22] Y. Cho, S. Pak, B. Li, B. Hou, S. Cha, *Adv. Funct. Mater.* **2021**, *31*, 2104239.

[23] Y. Cho, B. Hou, P. Giraud, S. Pak, S. Cha, *ACS Appl. Energy Mater.* **2021**, *4*, 12056.

[24] Y. Zhao, Q. Liao, G. Zhang, Z. Zhang, Q. Liang, X. Liao, Y. Zhang, *Nano Energy* **2015**, *11*, 719.

[25] P. Talemi, M. Delaigue, P. Murphy, M. Fabretto, *ACS Appl. Mater. Interfaces* **2015**, *7*, 8465.

[26] V. Cauda, S. Stassi, K. Bejtka, G. Canavese, *ACS Appl. Mater. Interfaces* **2013**, *5*, 6430.

[27] C. F. Groner, M. N. Hirsh, 1985 5th Int. Symp. on Electrets (ISE 5), Heidelberg, West Germany, September **1985**, 912.

[28] R. Liu, Q. Liu, D. He, G. Sun, Z. Li, Y. Zhu, *ACS Appl. Electron. Mater.* **2021**, *3*, 1804.

[29] M. C. Branciforti, V. Sencadas, S. Lanceros-Mendez, R. Gregorio Jr, *J. Polym. Sci., Part B: Polym. Phys.* **2007**, *45*, 2793.

[30] V. Sencadas, R. Gregorio Filho, S. Lanceros-Mendez, *J. Non-Cryst. Solids* **2006**, *352*, 2226.

[31] V. Bhavanasi, V. Kumar, K. Parida, J. Wang, P. S. Lee, *ACS Appl. Mater. Interfaces* **2016**, *8*, 521.

[32] J. Yan, Y. G. Jeong, *Compos. Sci. Technol.* **2017**, *144*, 1.

[33] M. Choi, G. Murillo, S. Hwang, J. W. Kim, J. H. Jung, C. Y. Chen, M. Lee, *Nano Energy* **2017**, *33*, 462.

[34] J. H. Li, X. S. Shao, Q. Zhou, M. Z. Li, Q. Q. Zhang, *Appl. Surf. Sci.* **2013**, *265*, 663.

[35] B. Li, C. Xu, J. Zheng, C. Xu, *Sensors* **2014**, *14*, 9889.

[36] A. Bouhamed, Q. Binyu, B. Böhm, N. Jöhrmann, N. Behme, W. A. Goedel, B. Wunderle, O. Hellwig, O. Kanoun, *Compos. Sci. Technol.* **2021**, *208*, 108769.

[37] A. Ince Yardimci, A. Durmus, M. Kayhan, O. Tarhan, *J. Macromol. Sci., Part B* **2022**, *61*, 749.

[38] D. Coelho, A. Sampaio, C. J. S. M. Silva, H. P. Felgueiras, M. T. P. Amorim, A. Zille, *ACS Appl. Mater. Interfaces* **2017**, *9*, 33107.

[39] Y. Mao, P. Zhao, G. McConohy, H. Yang, Y. Tong, X. Wang, *Adv. Energy Mater.* **2014**, *4*, 1301624.

[40] V. Jella, S. Ippili, J. H. Eom, J. Choi, S. G. Yoon, *Nano Energy* **2018**, *53*, 46.

[41] S. K. Ghosh, A. Biswas, S. Sen, C. Das, K. Henkel, D. Schmeisser, D. Mandal, *Nano Energy* **2016**, *30*, 621.

[42] R. Arumugam, P. Periakaruppan, *Int. J. Pharm. Sci. Res.* **2019**, *10*, 1439.

[43] W. Tyrra, *Heteroat. Chem.* **2002**, *13*, 561.

[44] G. I. N. Waterhouse, G. A. Bowmaker, J. B. Metson, *Phys. Chem. Chem. Phys.* **2001**, *3*, 3838.

[45] N. R. Chandra Raju, K. J. Kumar, A. Subrahmanyam, *J. Phys. D: Appl. Phys.* **2009**, *42*, 135411.

[46] J. R. Gregorio, M. Cestari, *J. Polym. Sci., Part B: Polym. Phys.* **1994**, *32*, 859.

[47] A. Arrigoni, L. Brambilla, C. Bertarelli, G. Serra, M. Tommasini, C. Castiglioni, *RSC Adv.* **2020**, *10*, 37779.

[48] E. Soergel, *J. Phys. D: Appl. Phys.* **2011**, *44*, 464003.

[49] M. Laurenti, S. Stassi, M. Lorenzoni, M. Fontana, G. Canavese, V. Cauda, C. F. Pirri, *Nanotechnology* **2015**, *26*, 215704.

[50] B. J. Rodriguez, C. Callahan, S. V. Kalinin, R. Proksch, *Nanotechnology* **2007**, *18*, 475504.